AIAA AVIATION Forum
22-26 June 2015, Dallas, TX
21st AIAA/CEAS Aeroacoustics Conference

10.2514/6.2015-3148

Check for updates

An experimental investigation of wall pressure fluctuations beneath pressure gradients

Édouard Salze*, Christophe Bailly†, Olivier Marsden‡, Emmanuel Jondeau§ and Daniel Juvé¶

Laboratoire de Mécanique des Fluides et d'Acoustique
École Centrale de Lyon & UMR CNRS 5509, 69134 Écully Cedex, France

I. Introduction

The understanding of the structural response under excitation is often the first motivation to study wall-pressure fluctuations. Vibrations and noise induced by turbulent-boundary-layer pressure is of importance in hydroacoustics,[3,7,26] but also in aeronautics[14,27] and more recently in automotive applications.[4,5,18] The aerodynamic part of wall-pressure fluctuations is associated with the indirect contribution to cabin noise through panel vibration while the acoustic part represents a direct contribution to this noise. Direct measurements of the wall pressure excitation by a turbulent boundary layer, including both aerodynamic and acoustic components of loading, is thus desirable. The large dynamic range between these two components makes this experimental characterization quite tricky.[2,11,12] Mainly the incompressible part of wall-pressure fluctuations has been reported over the past fifty years.[6,16] It must be mentioned that these difficulties are also encountered in numerical simulations.[13,15,17] Moreover, zero-pressure-gradient turbulent boundary layers are often considered, but numerous engineering applications involves the presence of pressure gradients. Only a fragmented view is currently offered regarding pressure gradient effects, even for modelling the aerodynamic loading.[8,20,25]

In a previous study by Arguillat *et al.*,[2] a rotating microphone array was used to estimate both the aerodynamic and the acoustic part of the wall pressure wavevector-frequency spectrum through an original post-processing. Results have been reported for a turbulent boundary layer at a Reynolds number $\mathrm{Re}_{\delta_\theta} = u_\tau \delta_\theta / \nu = 1716$ and at a moderate velocity $U_\infty = 44$ m.s^{-1} and the feasibility of obtaining pressure spectra by this original approach was demonstrated. In these expressions, u_τ denotes the friction velocity, δ_θ the momentum thickness and U_∞ the free stream velocity of the boundary layer, and ν is the kinematic viscosity of the fluid. It was also noticed that some improvements could be carried out in the future regarding the test channel as well as the antenna. Starting from this study, wall pressure fluctuations induced by a turbulent flow were investigated and the experimental approach was revisited and significantly improved. In the present work, two experimental set-ups were used to better describe wall-pressure features beneath a turbulent boundary layer.

First, a new channel was used for flow-acoustic measurements. The ceiling of the test section can be inclined, which allowed turbulent boundary layers in the presence of pressure gradients to be considered. A new disk antenna, mounted on a rigid flat plate, was also developed and carefully manufactured, to allow the determination of wall pressure wavevector-frequency spectra. Some properties of the turbulent flow for

*Research engineer, corresponding author, e-mail: edouard.salze@ec-lyon.fr
†Professor, AIAA senior member
‡Assistant professor
§Engineer
¶Professor, AIAA associate fellow

zero-pression-gradient boundary layers as well as for adverse- and favorable-pressure-gradient configurations, were reported in Salze *et al.*[24] Wall pressure fluctuations were also measured using a pinhole microphone combined to an original high-frequency calibration. They have been found in good agreement with previous experimental data. Direct measurements of wavevector-frequency spectra were performed with the use of a rotating linear antenna of remote microphones. The microphone distribution has been optimized to improve the array response with respect to previous works. The convection velocity or length scales associated with the aerodynamic contribution have been extracted from the data and compared to other measurements and some classical models. More recently, a wall jet facility was used for the optical characterization of the turbulent boundary layer. A particle image velocimetry technique was used to describe wall-bounded turbulence close to the wall.

In the present work, wavenumber-frequency spectra are rebuilt using all the properties of the rotating antenna, in order to extract the acoustic part. Furthermore, additional results are reported from an experiment in which cross-correlations between wall fluctuating pressure and the streamwise fluctuating velocity are measured in the presence of pressure gradients. particle image velocimetry snapshots are also analyzed to better understand wall-pressure fluctuations in the case of a wall jet excitation. The paper will be organized as follows. The experimental setups and techniques are described in section II. Results are presented and discussed in section III, and concluding remarks are given in section IV.

II. Experimental setups and techniques

The experiments were conducted in the main subsonic wind tunnel of the Centre Acoustique at Ecole Centrale de Lyon in France.[2, 22] The flow is generated by a 350 kW Neu centrifugal blower delivering a nominal mass flow rate of 15 kg.s^{-1}, and the fan is powered by an electronically controlled Tridge-Electric LAK 4280A motor. Air passes through a settling chamber including a honeycomb and several wire meshes designed to reduce free stream turbulence. The acoustic treatement on the wind tunnel walls and baffled silencers allows noise reduction, and prevents acoustic contamination of the measurements performed in the anechoic chamber. This results in an air flow at ambient temperature with a low background noise and low residual turbulence intensity, less than 1%.

II.A. The closed wind tunnel

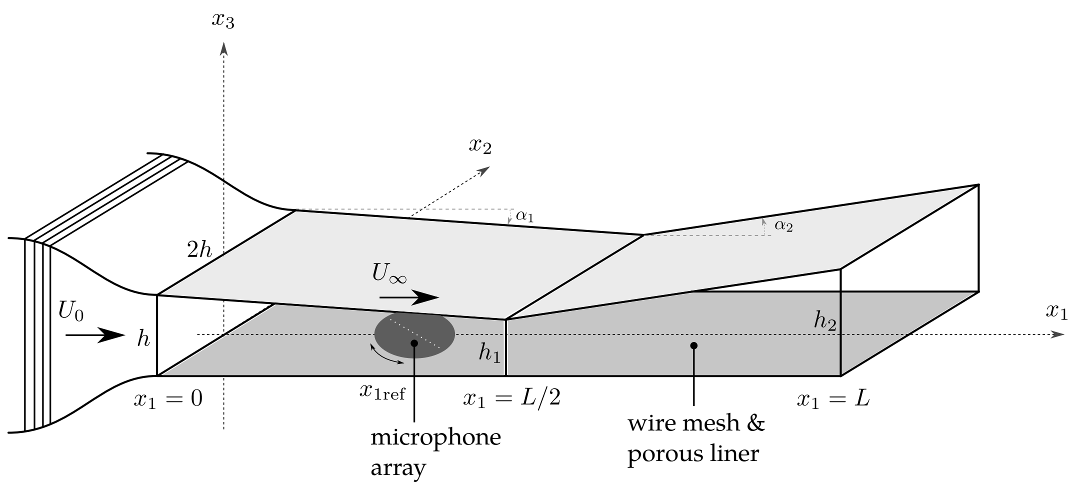

Figure 1. Sketch of the closed wind tunnel configuration and notations. The height of the initial section is $h = 250$ mm, the length of the closed wind tunnel is $L = 2$ m, and the location of the disk antenna is $x_{\mathrm{ref}} = 750$ mm. It should be noted that U_0 is the velocity at the channel inlet ($x_1 = 0$), and that U_∞ is the local free stream velocity of the boundary layer at the streamwise location of the measurement, $x_{1\mathrm{ref}}$ for the rotating antenna.

A sketch of the channel is shown in Figure 1. As mentioned in introduction, the two parts of the roof can be sloped to control the mean pressure gradient inside the channel. Three configurations were retained in the present study, corresponding to a turbulent boundary layer submitted to a zero-pressure-gradient, a favourable or negative pressure gradient and an adverse or positive pressure gradient. The side walls of the second part of the channel were acoustically treated using a wire mesh and a porous liner, in order to reduce noise generated by the jet at the channel outlet.

Velocity profiles inside the channel were measured using hot-wire anemometry, in particular to estimate the thickness and the friction velocity of the turbulent boundary layer. A complete characterization of the turbulent boundary layer was previously reported in Salze *et.al.*[24] and will not be reproduced here. The main parameters are indicated in Fig.1, were *zpg*, *apg* and *fpg* respectively denote a *zero*-, *adverse*- and *favourable*- pressure-gradient boundary layer. The last label *wj* denotes the wall jet experiment described in the next section.

	U_∞	$\delta_1 \times 10^3$	H	u_τ	Re_{δ_1}	Re^+	β
zpg	11	3.1	1.34	0.48	2.2×10^3	633	–
	25	2.8	1.30	1.02	4.7×10^3	1006	–
	36	3.2	1.30	1.35	7.4×10^3	1778	–
	45	3.7	1.31	1.65	1.1×10^4	2718	–
	59	3.6	1.31	2.05	1.4×10^4	3374	–
	76	2.9	1.28	2.71	1.5×10^4	3559	–
	100	3.5	1.30	3.54	2.3×10^4	5050	–
wj	50	2.8	1.37	1.73	9.6×10^3	3309	–
apg	8	8.4	1.38	0.31	4.6×10^3	1036	0.95
	12	8.2	1.42	0.42	6.7×10^3	1122	1.06
	19	6.2	1.41	0.66	7.9×10^3	1321	0.83
	27	5.0	1.36	0.96	9.1×10^3	1596	0.64
	38	5.5	1.31	1.34	1.4×10^4	3555	0.71
	45	5.8	1.31	1.55	1.8×10^4	5135	0.81
	57	5.2	1.31	1.95	2.0×10^4	5139	0.72
	76	6.0	1.31	2.45	3.0×10^4	8027	0.94
fpg	10	2.1	1.27	0.50	1.5×10^3	501	−0.48
	32	2.1	1.24	1.35	4.6×10^3	1353	−0.63
	45	1.7	1.23	1.90	5.0×10^3	1881	−0.50
	63	1.8	1.22	2.53	7.5×10^3	2490	−0.59

Table 1. Boundary layer parameters for the present experiments at ECL.

II.B. Wall-pressure instrumentation and signal processing

The principle of a linear array of 63 pressure sensors placed on a rotating disk inside the closed wind tunnel has again been retained for this study. With respect to the study in Arguillat *et al.*,[2] the diameter of the disk has been slightly increased to obtain a better resolution of low frequency components. Moreover a non-uniform radial distribution of the probes has also been chosen. An accurate description of the aerodynamic ridge requires a very small distance between probes, of the order of one millimeter, which can unfortunately not be obtained by using flush-mounted 1/4 or 1/8 inch microphones. Remote microphones have thus been selected in this work, even if this solution also presents some drawbacks. Wall pressure fluctuations have also been measured using a pinhole microphone combined to an original high-frequency calibration.[24] Following Corcos,[9] all pressure spectra obtained using the pinhole microphone have been corrected to account for the spatial filtering of the sensor. Unsteady pressure signals are simultaneously recorded over the 63 probes at a sampling frequency of 51.2 kHz during a time period of $T_0 = 90$ s.

The Fourier transform $\hat{p}(\boldsymbol{k},\omega)$ of the pressure field $p(\boldsymbol{x},t)$ in space and in time is defined by

$$p(\boldsymbol{x},t) = \iint \hat{p}(\boldsymbol{k},\omega) e^{i(\boldsymbol{k}\cdot\boldsymbol{x}-\omega t)} d\boldsymbol{k} d\omega = \mathcal{F}^{-1}\left\{\hat{p}(\boldsymbol{k},\omega)\right\}$$

Assuming stationary random signals and ergodicity, the cross spectral density is defined as,

$$R_{pp}(\boldsymbol{x},\boldsymbol{\xi},\omega) = \lim_{T\to\infty} \frac{2\pi}{T} E\big[\hat{p}(\boldsymbol{x},\omega)\hat{p}^{\star}(\boldsymbol{x}+\boldsymbol{\xi},\omega)\big]$$

where $\boldsymbol{\xi} = (\xi_1,\xi_2)$ is the separation vector between two probes located at $\boldsymbol{x}$ and $\boldsymbol{x}+\boldsymbol{\xi}$. The cross-spectra R_{pp} are extracted from time signals using 360 blocks of time length $T = 250$ ms with no overlap between the blocks. In practice, the wall pressure field is assumed to be homogeneous over the microphone array, that is $R_{pp}(\boldsymbol{x},\boldsymbol{\xi},\omega) = R_{pp}(\boldsymbol{\xi},\omega)$. The wavevector-frequency spectrum is then directly computed by discretizing the following Fourier integral,

$$\Phi(\boldsymbol{k},\omega) = \frac{1}{(2\pi)^2} \iint R(\boldsymbol{\xi},\omega) e^{-i\boldsymbol{k}\cdot\boldsymbol{\xi}} d\boldsymbol{\xi} \tag{1}$$

A similar approach was developed previously by some of the present authors,[2,24] using the central probe as a reference sensor. For each of the 64 angular positions reached by the rotating antenna, 63 cross-spectra between sensors were computed in the cross-spectral matrix (see Fig. 2 at left).

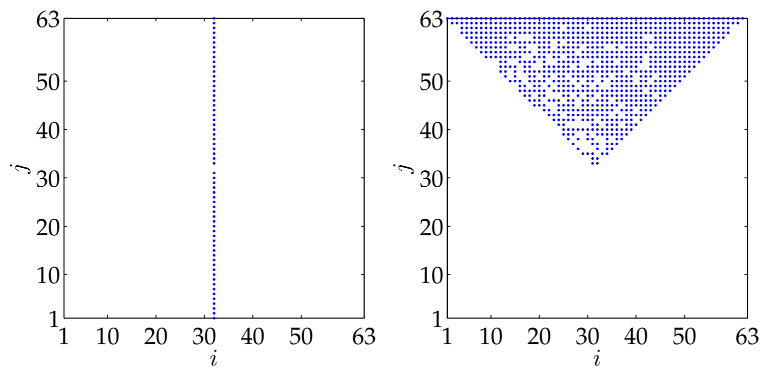

Figure 2. Cross-spectral matrix (CSM) of the rotating antenna, for a single angular position. At left: referenced CSM, at right: full CSM. A blue dot indicates that a cross-spectrum between sensors i and j is used in the calculation.

The Fourier integral (1) was then computed directly over 63×64 spatial positions, in polar coordinates. In the present work, all the possible cross-spectra between sensors have been computed in order to enrich the spatial discretizing of the quantity $R(\boldsymbol{\xi},\omega)$. Given the symmetry property of the cross-spectral matrix:

$$R_{ij} = {R_{ji}}^{\star}$$

the symetry property of the linear array:

$$R_{i',j'} = R_{2N_0-j,2N_0-i}$$

and the possible doublings of ξ vectors, the Fourier integral (1) was now computed over 855×64 spatial positions in polar coordinates (see Fig. 2 at right). This procedures doubles the spectral resolution of the rotating antenna, a better description of the acoustic part of the wavevector spectrum if therefore expected.

An 1/8 inch Brüel & Kjær type 4138 microphone was also used to obtain one-point frequency spectra. The sensing area of the microphone has been reduced by fitting it with a pinhole mask made of a perforated cap. The diameter of the pinhole is about $d_p \simeq 0.5$ mm. An original calibration procedure was developed, in order to describe frequency spectra up to 50 kHz.[24] During the closed wind tunnel experiment, the pinhole microphone was located on the rotating disk (see Fig.1). During the wall jet experiment, the pinhole microphone is located at the center of the PIV window, 400 mm downstream from the nozzle exit, see Fig.3.

II.C. The wall jet

A sketch of the wall jet facility is shown in Fig.3. The flow is guided through a rectangular nozzle with a cross section of 250 by 500 mm over a wooden flat plate measuring 600 mm in the cross-flow direction by 1.2 m in the streamwise direction. The measurement section for the PIV set-up is located 400 mm downstream from the nozzle exit, well inside the potential core of the wall jet. The turbulent boundary layer has first been characterized using hot-wire anemometry. The main parameter resulting from this characterization are detailed in Table 1, were the label *wj* denotes the wall jet configuration. It should be noted that, in the wall jet experiment, U_∞ denotes the maximum velocity of the wall jet above the turbulent boundary layer. The outer region of the wall jet, where the velocity tends to zero, is much higher and was therefore not investigated in this study.

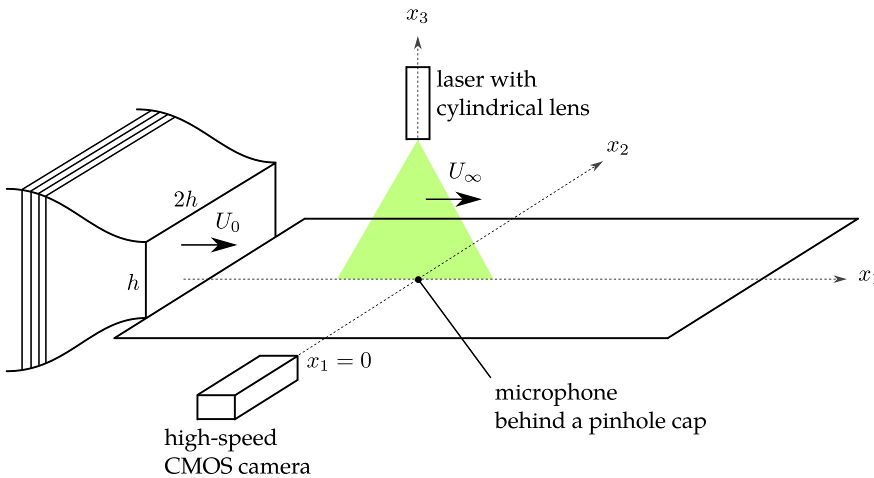

Figure 3. Sketch of the wall jet configuration and notations. The height of the initial section is $h = 250$ mm, the length of the flat plate is 600 mm, and the pinhole microphone is located 400 mm downstream from the nozzle exit.

Velocity profiles are reported in Fig.4. Mean and fluctuating components have been extracted both from hot-wire measurements and from the PIV snapshots at $x_1 = 0$ as a function of x_3. The mean velocity profile extracted from hot-wire measurements (see Fig.4, left) exhibits a plateau far from the boundary (${x_3}^+ > 2000$) and a classical logarithmic region (${x_3}^+ < 500$). The outer region where the mean velocity vanishes is not visible. The velocity profile is therefore very close in shape to a closed wind tunnel boundary-layer velocity profile. A very good agreement (within 3%) between PIV measurements and hot-wire measurements is obtained. However, because of light diffusion, the region ${x_3}^+ < 300$ cannot be determined using the present PIV setup.

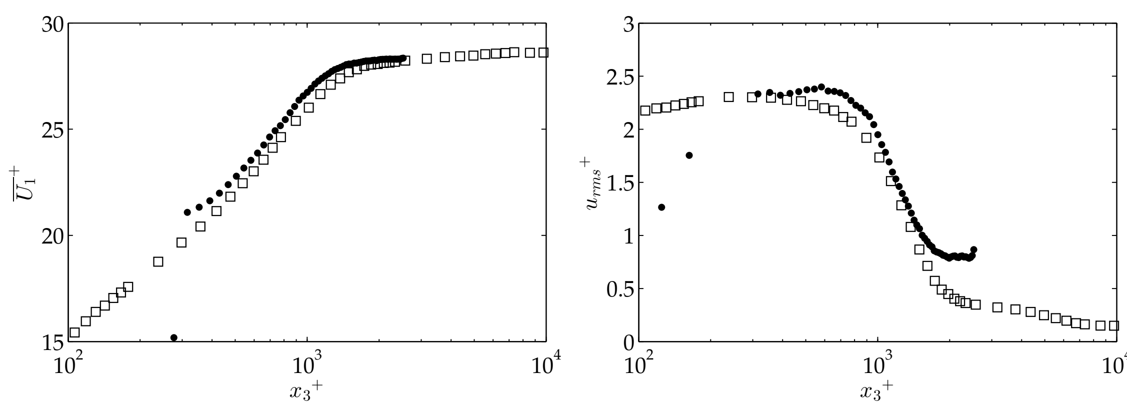

Figure 4. At left : mean velocity profile $\overline{U_1}$ as a function of x_3. At right : velocity fluctuations u^+_{rms} as a function of x_3. □ : hot-wire measurements, • : PIV measurements.

II.D. Particle Image Velocimetry

Thurbulent velocity fields were obtained in the boundary layer by a two-dimensional two-components time-resolved particle image velocimetry technique (see Fig. 3). A SAFEX smoke generator was used to create glycol particles of size 1 μs to seed the flow. A CMOS Phantom V12 camera with a dynamic range of 12 bits and a resolution of 1280×800 pixels was used to obtain 68×21 mm snapshots of the boundary layer. Images were corrected for possible optical distortions. A vertical sheet of the turbulent flow was illuminated using a Quantronix Darwin Duo Nd–YLF dual-cavity laser with a pulse energy of 18 mJ and a 527 nm wavelength. The two laser cavities were ignited with a time delay of 10 μs, resulting pairs of images. LaVision DaVis v7.2 software was used to compute flow fields from these pairs of images by multipass correlation. An interrogation window of 64×64 pixels is first considered, and then reduced to 12×12 pixels with an overlap of 50%. A dataset consists of 5540 pairs of images at a repetition rate of 6.2 kHz, during a time period of 0.89 s. A total of 10 datasets were recorded during the experimental campaign.

III. Results and discussion

III.A. Wavenumber-frequency spectra

Cross-spectra and wavevector-frequency spectra were extracted from the rotating antenna signals using the method described in section II.B. In this section, interest is focused on the zpg45 and fpg32 cases (see Table 1) for the same reduced frequency $\omega\delta_1/U_\infty = 0.5$. This frequency corresponds to the maximum of energy measured in the point spectra.[24] . Two examples of two-dimensional cross-spectral densities $R(\boldsymbol{\xi})$ are represented in Fig. 5. In these figures, black dots represent the cross-spectral quantity $R(\boldsymbol{\xi})$ at each of the 855×64 calculation points (see section II.B). Red dots were used to highlight the cross-spectrum in the streamwise direction, whereas blue dots were used for the spanwise direction. The loss of coherence in the spanwise direction is faster than in the streamwise direction. Following Corcos,[10] the decay can be described with an excellent agreement by an exponential profile. In a previous study,[24] empirical expressions for the coherence length were proposed and tabulated with respect to the pressure gradient.

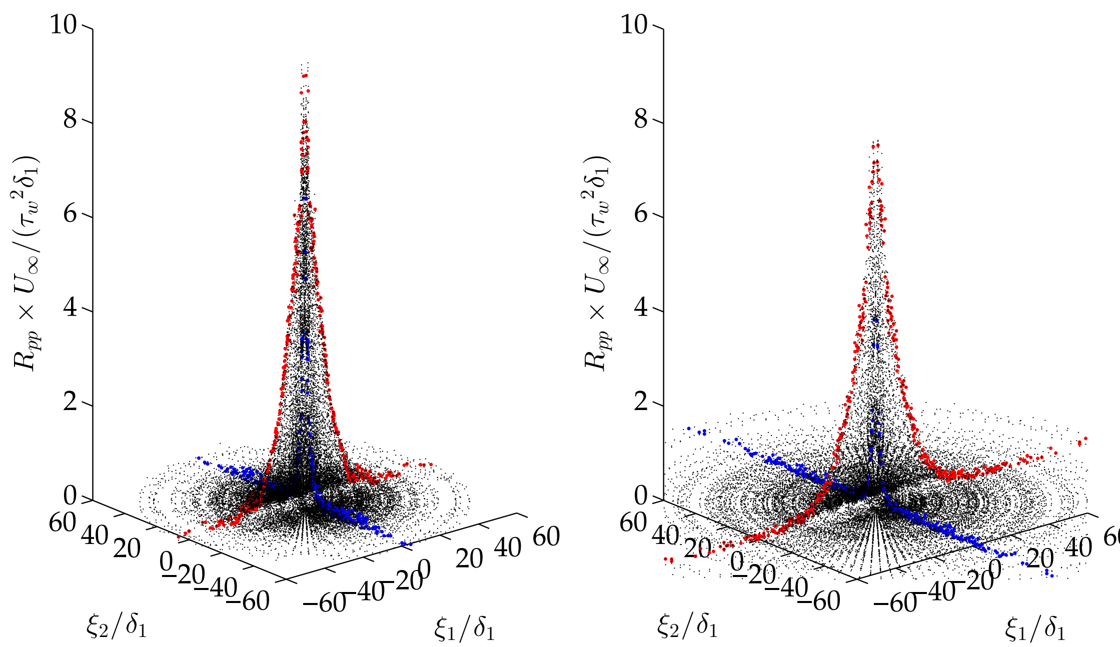

Figure 5. Two-dimensional cross-spectral density $R(\boldsymbol{\xi},\omega) \times U_\infty/(\tau_w{}^2\delta_1)$ for $\omega\delta_1/U_\infty = 0.5$. At left: zpg45 case. At right: fpg32 case.

The corresponding wavevector-frequency spectra, obtained from a spatial Fourier transform of the cross-spectra are plotted in Fig. 6. The incompressible contribution to wall-pressure fluctuations is clearly visible around the convective wavenumber $k_1 = k_c = \omega/U_c$, with an elongated shape in the k_2 direction. The dissymmetry of the convective ridge in the k_1 direction is also apparent. Compared to the zero-pressure-gradient case, the convective ridge of the favourable-pressure-gradient case is smaller in the k_1 direction. This is coherent with the two-dimensional cross-spectra shown in Fig. 5, where the wall-pressure field was found more coherent in the k_1 direction in the fpg32 case than in the zpg45 case. This is also an indication of a streamwise elongation of the turbulent structures in the boundary layer submitted to a favourable pressure gradient. On the colormaps, an acoustic component is also identified in the low wavenumbers region. The relative contribution of the compressible part is higher in the fpg case than in the zpg case, of the order of 1%. The proper extraction of the acoustic part is currently examined and requires further analysis.

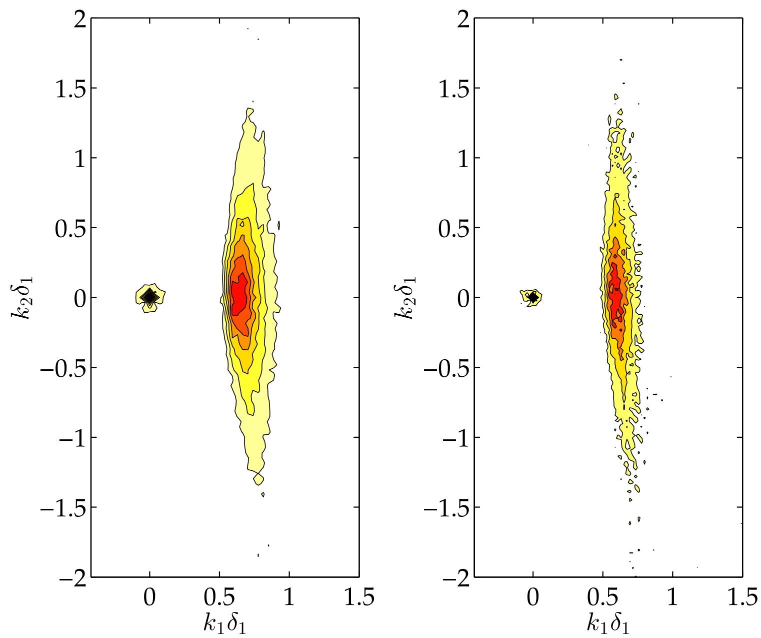

Figure 6. Two-dimensional wavenumber-frequency spectra $\Phi_{pp}(\boldsymbol{k}, \omega) \times U_\infty/({\tau_w}^2 {\delta_1}^3)$ for $\omega\delta_1/U_\infty = 0.5$. At left: zpg45 case. At right: fpg32 case.

III.B. Particle image velocimetry snapshots

Three successive examples of PIV snapshots are reported in Fig.7. Following previous work,[1] these snapshots have been obtained by substracting from the instantaneous velocity field $\boldsymbol{u}(x_1, x_3)$ a fraction of the free-stream velocity, here $0.85\,U_\infty$. This procedure reveals vortices travelling in the boundary layer at the specified convection velocity. Moreover, these snapshots have been colored by the vorticity magnitude $|\omega_2|$ to make easier the visual identification of turbulent structures. In order to obtain clean vorticity maps, the two-dimensional Fourier transform was computed for each velocity field, and a gaussian low-pass filter was applied. The filter width was set to 2×10^3 rad/m in order to remove the smallest structures. Finally, the two-dimensional inverse Fourier transform was computed, and the vorticity maps were finally computed from the filtered velocity fields.

Using a convection velocity of $0.85\,U_\infty$ reveals the structure of the boundary layer at a height of about $500 < {x_3}^+ < 1000$. In this region, a typical turbulent eddie will have a diameter of about 200^+. The field of vorticity is well related to rotational structures made apparent by this Galilean decomposition. Similarly to Adrian,[1] large hairpin vortices are observed in the boundary layer (see for example Fig.7, third snapshot, around ${x_1}^+ = 1600$, ${x_3}^+ = 600$), at local maxima of vorticity.

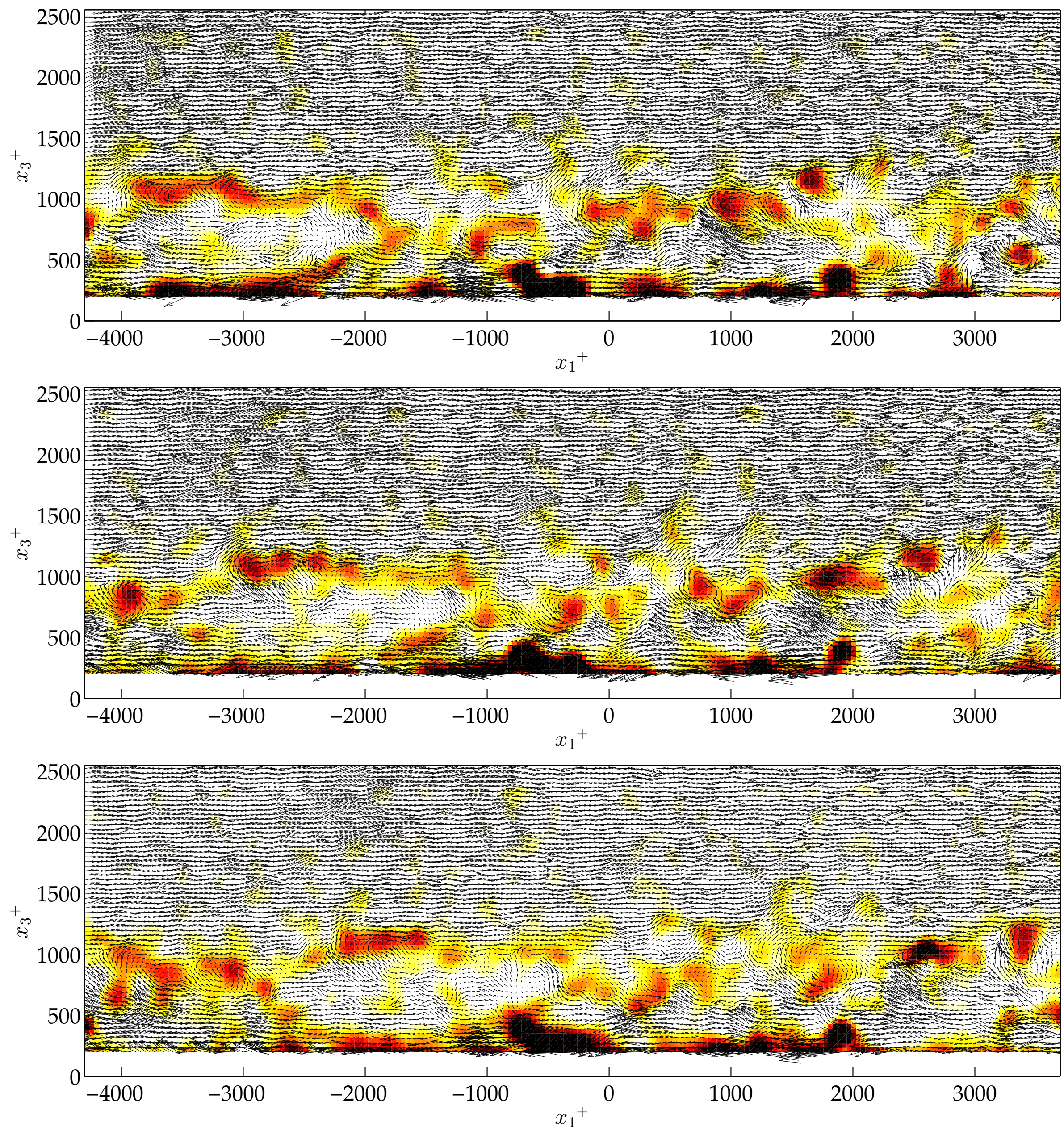

Figure 7. Three successive snapshots of the velocity field $\boldsymbol{u}(x_1, x_3) - U_c$ with $U_c = 0.85\, U_\infty$, colored by vorticity magnitude $|\omega_2|$ (161 μs between two successive snapshots).

III.C. Wall-pressure – velocity correlations

A 1/8 inch Brüel & Kjær type 4138 microphone has been used to measure pressure-velocity correlations. The sensing area of the microphone has been reduced by fitting it with a pinhole mask made of a perforated cap. The diameter of the pinhole is about $d_p \simeq 0.5$ mm. A Streamline anemometer combined with a Dantec 55P01 hot-wire operating in constant voltage mode provides the streamwise velocity. The probe is located above the pinhole microphone, as shown in Figure 8, and can be moved from $x_3 = 0.1$ mm to a distance $x_3 = 12$ cm from the wall. The displacement of the hot-wire probe is performed using a motorized device.

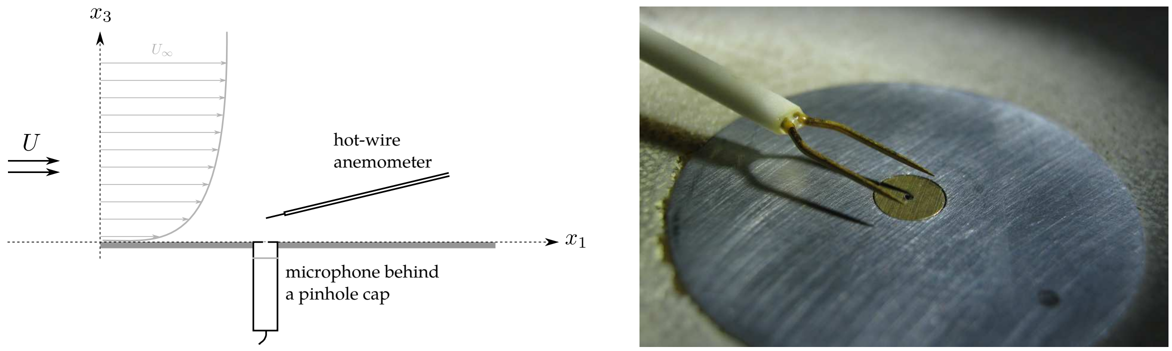

Figure 8. On the left, sketch of the experimental setp-up. On the right, picture of the hot wire anemometer just above the pinhole microphone.

The cross-spectral density between the fluctuating wall pressure $p(x_3 = 0, t)$ and the streamwise velocity $u_1(x_3, t)$ is defined by

$$R_{p,u_1}(x_3, \omega) = \lim_{T \to \infty} \frac{2\pi}{T} E\big[\hat{p}(\omega)\hat{u}_1^\star(x_3, \omega)\big]$$

where E denotes the expected value, and T is the time length of signals. This cross spectrum is normalized as a coherence function denoted γ_{p,u_1}, given by

$$\gamma_{p,u_1}(x_3, \omega) = \sqrt{\frac{|R_{p,u_1}(x_3, \omega)|^2}{S_{pp}(\omega) S_{u_1 u_1}(x_3, \omega)}}$$

where $S_{pp}(\omega) = R_{p,p}(\omega)$ and $S_{u_1 u_1}(x_3, \omega) = R_{u_1,u_1}(x_3, \omega)$ are the pressure and velocity spectra, respectively. Pressure and velocity signals are simultaneously recorded at a sampling frequency of 100 kHz during a length time $T_0 = 90$ s. The periodogram method is performed for the averaging of the spectral quantities, using 360 time blocks of length $T = 250$ ms, with no overlap. Low frequencies, namely below 100 Hz, are disregarded in what follows.

As an illustration, the coherence function γ_{p,u_1} normalized by inner variables, is plotted in Figure 9 as a function of the position ${x_3}^+ = x_3 u_\tau / \nu$ and of the frequency $\omega^+ = \omega\nu / {u_\tau}^2$, and for the configurations apg38, zpg45 et fpg63. Coherence decreases with the distance x_3 and the frequency for the three cases. The maximum is of about 20% for the apg38 configuration, 24% for the zpg45 configuration and 33% for the fpg63 configuration. This maximum is reached for different values of the distance from the wall, ${x_3}^+ = 450$ for the apg38 case, ${x_3}^+ = 340$ for the zpg45 and fpg63 cases, but approximately for the same frequency $\omega^+ \simeq 0.005$. The peak of coherence can be parametrized by the following empirical expression

$$ {x_3}^+ = {\delta_1}^+ \exp\left(\omega^+ / \Omega_0\right) \tag{2}$$

where the constant Ω_0 is a function of the pressure gradient, $\Omega_0 = 0.067$ for the apg38 case, $\Omega_0 = 0.083$ for the zpg45 case and $\Omega_0 = 0.091$ for the fpg63 case. This expression corresponds to the white solid line in Figure 9. The spot of maximum coherence in the region $300 < {x_3}^+ < 1000$ can be associated to the existence of large-scale structures in the boundary layer (see Fig. 7).

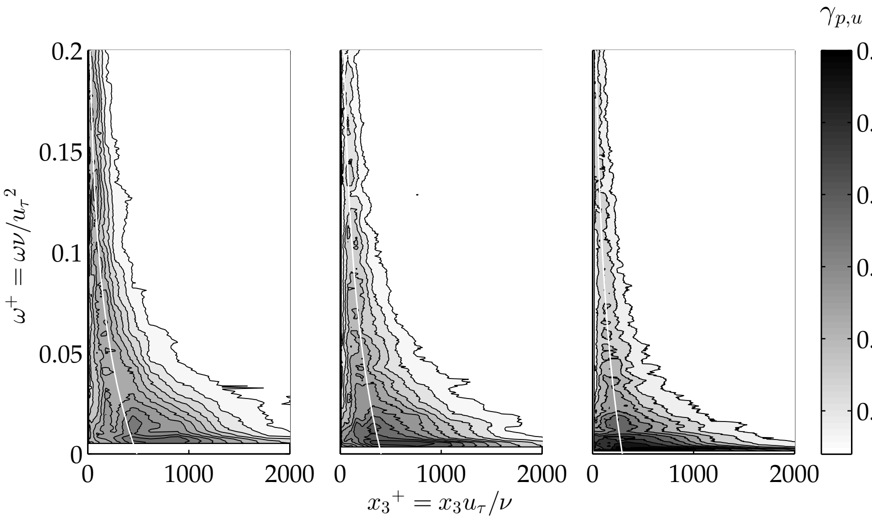

Figure 9. Coherence function γ_{p,u_1} between wall pressure and streamwise velocity as a function of the distance from the wall $x_3{}^+$ and of the frequency ω^+. Ten isocontours are plotted such as $0.02 < \gamma_{p,u_1} < 0.3$. On the left, apg38 case; on the middle, zpg45 case and on the right, fpg63 case. The white solid line corresponds to the peak of coherence determined by Eq. (2).

IV. Concluding remarks

Wall-pressure measurements have been performed using a linear array of remote microphone probes.[24] In this paper, wavevector-frequency spectra have been extracted using all the possible spacings between probes, in order to enhance the representation of the cross-spectral components. An acoustic component and an incompressible contribution are identified. Effects induced by the presence of a mean pressure gradient has been highlighted. The proper extraction of the acoustic contribution is still examined and requires further investigation. A preliminary particule image velocimetry experiment has also been performed on a wall jet boundary layer, with similar characteristics. Large scale vortices are identified in a region where pressure–velocity coherence is maximum. The region of maximum coherence between pressure and velocity has been described using an empirical law, and a parametrization seems possible. Future work will focus on the extraction of wall-pressure quantities using particule image velocimetry. The comparison of our experimental database to numerical simulations will help the modelling of wall-pressure wavevector-frequency spectra in the future.

Acknowledgments

This research has been funded by the Agence Nationale de la Recherche through the ANR-2011-BS09-035-02 project SONOBL, and also by the Labex CeLyA of Université de Lyon, operated by the French National Research Agency (ANR-10-LABX-0060/ ANR-11-IDEX-0007). The authors wish to express their most sincere thanks to Pascal Souchotte, Nathalie Grosjean, Jean-Michel Perrin and Pierre Roland for their help in setting up the experiment.

A. Nomenclature

h	height of the channel
$H = \delta_1/\delta_\theta$	shape factor
$\boldsymbol{k}$	wavevector ($\boldsymbol{k} \in \mathbb{R}^3$)
p_w	wall pressure

$q_0 = \rho U_0^2/2$	dynamic pressure
$\mathrm{Re}_{\delta_1} = U_\infty \delta_1/\nu$	Reynolds number based on δ_1
$\mathrm{Re}^+ = u_\tau \delta/\nu$	Kármán or friction Reynolds number
$\boldsymbol{r}$	separation vector (polar coordinates)
$R_{pp}(\boldsymbol{r}, \omega)$	pressure cross spectral density
$S_{pp}(\omega) = R_{pp}(\boldsymbol{r} = 0, \omega)$	one-sided wall pressure spectrum
U_0	inlet velocity (at $x_1 = 0$)
U_∞	local free-stream velocity at $x_{1\mathrm{ref}}$
U_c	convection velocity
u_τ	friction velocity
$\boldsymbol{x} = (x_1, x_2, x_3)$	Cartesian coordinates, see Fig. 1 and 3
$\beta = (\delta_1/\tau_w) dP_e/dx_1$	Clauser parameter
δ	boundary layer thickness
δ_1	boundary layer displacement thickness
δ_θ	boundary layer momentum thickness
$\gamma(\boldsymbol{\xi}, \omega)$	coherence function
$\omega_{\delta_1} = \omega \delta_1/U_\infty$	dimensionless angular frequency
$\Phi_{pp}(\boldsymbol{k}, \omega)$	wavevector-frequency wall pressure spectrum
$\tau_w = \rho u_\tau^2$	wall shear stress
$\boldsymbol{\xi}$	separation vector

The superscript + denotes a dimensionless quantity using viscous scaling, e.g. $x_3^+ = x_3 u_\tau/\nu$, and $\star$ a complex conjugate.

References

[1] Adrian, R.J., Meinhart, C.D., & Tomkins, C.D., 2000, Vortex organization in the outer region of the turbulent boundary layer, *J. Fluid Mech.*, **422**, 1–54.

[2] Arguillat, B., Ricot, D., Bailly, C. & Robert, G., 2010, Measured wavenumber - frequency spectrum associated with acoustic and aerodynamic wall pressure fluctuations, *J. Acoust. Soc. Am.*, **128**(4), 1647–1655.

[3] Blake, W.K., 1986, Essentials of turbulent wall-pressure fluctuations, in Mechanics of flow-induced sound and vibration, Vol. II Complex flow-structure interactions, *Academic Press Inc.*, Orlando, Florida.

[4] Bremner, P.G., 2012, Vibroacoustic source mechanisms under aeroacoustic loads, AIAA Paper 2012-2206.

[5] Bremner, P.G., 2014, Developing aerodynamic design diagnostics for control of interior wind noise, Proceedings of the 14ème Congrès Français d'Acoustique, 22-25 avril, Poitiers, France, 2139-2146.

[6] Bull, M.K., 1996, Wall-pressure fluctuations beneath turbulent boundary layers: some reflections on forty years of research, *J. Sound Vib.*, **190**(3), 299–315.

[7] Catlett, M.R., Forest, J.B., Anderson, J.M. and Stewart, D.O., 2014, Empirical spectral model of surface pressure fluctuations beneath adverse pressure gradients," 20th AIAA/CEAS Aeroacoustics Conference, AIAA Paper 2014-2910.

[8] Cipolla, K. & Keith, W., 2000, Effects of pressure gradients on turbulent boundary layer wave number frequency spectra, *AIAA Journal*, **38**(10), 1832–1836.

[9] Corcos, G. M., 1963, Resolution of pressure in turbulence, *J. Acous. Soc. Am.*, **35**(2), 192–199.

[10] Corcos, G. M., 1964, The structure of the turbulent pressure field in boundary-layer flows, *J. Fluid Mech.*, **18**(3), 353–378.

[11] Ehrenfried, K. & Koop, L., 2008, Experimental study of pressure fluctuations beneath a compressible turbulent boundary layer, 14th AIAA/CEAS Aeroacoustics Conference, AIAA Paper 2008-2800.

[12] Gabriel, C., Müller, S., Ullrich, F. & Lerch, R., 2014, A new kind of sensor arry for measuring spatial coherence of surface pressure on a car's side window, *J. Sound Vib.*, **333**, 901–915.

[13] Gloerfelt, X. & Berland, J., 2013, Turbulent boundary-layer noise: direct radiation at Mach number 0.5, *J. Fluid Mech.*, **723**, 318–351.

[14]Graham, W. R., 1997, A comparison of models for the wavenumber-frequency spectrum of turbulent boundary layer pressures, *J. Sound Vib.*, **206**(4), 430–454.

[15]Hu, Z., Morfey, C. L. & Sandham, N. D., 2006, Sound radiation from a turbulent boundary layer, *Phys. Fluids*, **18, 098101**, 1–4.

[16]Keith, W. L., Hurdis, D. A. & Abraham, B. M., 1992, A comparison of turbulent boundary layer wall-pressure spectra, *Journal of Fluids Engineering*, **114**, 338–347.

[17]Kremer, F., Bogey, C. & Bailly, C., 2014, Semi-implicit Runge-Kutta schemes: development and application to compressible channel flow, *AIAA Journal*, **52**(3), 516–527.

[18]Leclercq, D. J. J. & Bohineust, X., 2002, Investigation and modelling of the wall pressure field beneath a turbulent boundary layer at low and medium frequencies, *J. Sound Vib.*, **257**(3), 477–501.

[19]Maidanik, G., 1967, Flush-Mounted pressure transducer systems as spatial and spectral filters, *J. Acoust. Soc. Am.*, **42**(5), 1017–1024.

[20]McGrath, B. E. & Simpson, R. L., 1987, Some features of surface pressure fluctuations in turbulent boundary layers with zero and favorable pressure gradients, NASA-CR-4051.

[21]Nélisse, H. & Nicolas, J., 1997, Characterization of a diffuse field in a reverberant room, *J. Acoust. Soc. Am.*, **101**(6), 3517–3524.

[22]Panton, R. L. & Robert, G., 1994, The wavenumber-phase velocity representation for the turbulent wall-pressure spectrum, *Journal of Fluid Engineering*, **480**(116), 477–483.

[23]Rozenberg, Y., Robert, G. & Roger, M., 2012, Wall-pressure spectral model including the adverse pressure gradient effects, *AIAA Journal*, **50**(10), 2168–2179.

[24]Salze, E., Bailly, C., Marsden, O., Jondeau, E. and Juvé, D., 2014, An experimental characterization of wall pressure wavenumber-frequency spectra in the presence of pressure gradients, AIAA/CEAS Aeroacoustics Conference, AIAA Paper 2014-2909.

[25]Schloemer, H. H., 1967, Effects of pressure gradient on turbulent-boundary-layer wall-pressure fluctuations, *J. Acoust. Soc. Am.*, **42**(1), 93–113.

[26]Sevik, M. M., 1986, Topics in hydro-acoustics, in *Aero- and Hydro-Acoustics*, Springer-Verlag Berlin, 285–308.

[27]Wilby, J. F., 1996, Aircraft interior noise, *J. Sound Vib.*, **190**(3), 545–564.